

# The Effectiveness of Mid IR / Far IR Blind, Wide Area, Spectral Surveys in Breaking the Confusion Limit

Gwenifer Raymond<sup>\*1</sup>, Kate G. Isaak<sup>1</sup>, Dave Clements<sup>2</sup>, Adam Rykala<sup>1</sup>, Chris Pearson<sup>3,4</sup>  
<sup>\*</sup> *gwenifer.raymond@astro.cf.ac.uk*

<sup>1</sup> *Cardiff University, School of Physics & Astronomy, Queens Buildings, The Parade, Cardiff, CF24 3AA, UK*

<sup>2</sup> *Astrophysics Group, Blackett Laboratory, Imperial College, Prince Consort Road, London, SW7 2BW, UK*

<sup>3</sup> *Space Science and Technology Department, CCLRC Rutherford Appleton Laboratory, Didcot, Oxfordshire OX11 0QX, UK*

<sup>4</sup> *Department of Physics, University of Lethbridge, 4401 University Drive, Lethbridge, Alberta T1J 1B1, Canada*

(Received (15-05-09); accepted (20-03-10))

## Abstract

Source confusion defines a practical depth to which to take large-area extragalactic surveys. 3D imaging spectrometers with positional as well as spectral information, however, potentially provide a means by which to use line emission to break the traditional confusion limit. In this paper we present the results of our investigation into the effectiveness of mid/far infrared, wide-area spectroscopic surveys in breaking the confusion limit. We use SAFARI, a FIR imaging Fourier Transform Spectrometer concept for the proposed JAXA-led SPICA mission, as a test case. We generate artificial skies representative of 100 SAFARI footprints and use a fully-automated redshift determination method to retrieve redshifts for both spatially and spectrally confused sources for bright-end and burst mode galaxy evolution models. We find we are able to retrieve accurate redshifts for 38/54% of the brightest spectrally confused sources, with continuum fluxes as much as an order of magnitude below the 120  $\mu\text{m}$  photometric confusion limit. In addition we also recover accurate redshifts for 38/29% of the second brightest spectrally confused sources. Our results suggest that deep, spectral line surveys with SAFARI can break the traditional photometric confusion limit, and will also not only resolve, but provide redshifts for, a large number of previously inaccessible galaxies. To conclude we discuss some of the limitations of the technique, as well as further work.

## 1. Introduction

The cosmic infrared background (CIB) peaks at  $\sim 150 \mu\text{m}$  and comprises the total infrared (IR) emission from all sources in the sky (eg. Dole et al. 2001, Elbaz et al. 2002), integrated over all time. It has been found to contain as much energy as the combined optical/UV extragalactic background, suggesting that half of all light emitted by stars and active galactic nuclei (AGN) is absorbed by dust before we are able to observe it in the optical (Hauser & Dwek 2001). Locally, the IR output of typical galaxies is only one third of their optical output (Soifer & Neugebauer 1991), which implies strong evolution in the IR properties of galaxies as one moves to high redshift. The CIB has been well-studied using many instruments including ISOCAM (ISO), MIPS (Spitzer), ISOPHOT (ISO) and SCUBA(JCMT) at 15, 24, 160 and 850  $\mu\text{m}$  (Elbaz et al. 2002, Papovich et al. 2004, Juvela et al. 2000 and Smail et al. 2002 respectively). Although the peak of the CIB lies at  $\sim 150 \mu\text{m}$ , it has yet to be resolved into individual sources at these wavelengths: our understanding of the make-up of the CIB therefore relies on extrapolation.

Observations in the mid and far-infrared (MIR and FIR; typically defined as lying in the wavebands 5-30 and 30-1000  $\mu\text{m}$  respectively) from ground based telescopes are difficult if not impossible because of the high opacity of the Earth's atmosphere at these wavelengths. Ground based

telescopes are only sensitive to narrow wavebands in the MIR/FIR where the atmosphere's transmission is higher, thus wide band observations in the MIR/FIR must typically be made from space. As a result, FIR telescopes are smaller in diameter than their optical counterparts (up to a few meters), with a resulting angular resolution that is low compared to both optical and radio telescopes/interferometers. A direct consequence of this low angular resolution is that completely resolving the CIB into discrete sources in the FIR is very difficult, if not impossible, because of source confusion.

Source confusion may be defined as the degradation of the quality of photometry of sources clustered on a scale to the order of the telescope beam size (eg. Scheuer 1957). The confusion limit sets the useful depth to which large-area extra-galactic surveys should be taken. For example, the Herschel mission (Pilbratt 2004), successfully launched in May 2009, has a 3.5 m diameter mirror which realizes an angular resolution of 8" at 120  $\mu\text{m}$ . At these wavelengths, the confusion limit for such a mirror is estimated to be around  $\sim 5 \text{ mJy}$  (eg. Dole et al. 2004, Jeong et al. 2006). Surveys at 24  $\mu\text{m}$  suggest that at these flux levels one will only be able to resolve at most  $\sim 50\%$  of the CIB (Dole et al. 2004). It is possible to reduce the confusion limit through making observations with a larger diameter mirror. However, due to the practical limitations of high angular resolution FIR imaging there is a limit on how much we can reduce confusion noise.

One way to break the confusion limit makes use of the extra dimension of wavelength, to which one has access in spectroscopic surveys. Discrete sources can be identified by relatively bright, narrow-band emission lines: thereby allowing redshifts to be determined. A preliminary study to explore the efficacy of blind, wide area spectroscopic surveys in resolving FIR sources is described in Clements et al. (2007). In their work an artificial ‘sky’ was populated using template FIR spectral energy distributions (SEDs) of a selection of different types of galaxy, to which were added FIR emission lines of strengths derived from ISO-LWS observations (eg. Negishi et al. 2001). The sources were redshifted and assigned luminosities according to the evolutionary models of Pearson (2005), Pearson et al. (2007) and Pearson & Khan (2009). Observations of the ‘sky’ were made using the instrumental parameters (eg. sensitivity/noise levels, spectral resolution, field of view (FoV), beam size) of SAFARI, a FIR imaging Fourier Transform Spectrometer concept for the proposed JAXA-led SPICA (Space Infrared Telescope for Astronomy and Astrophysics) (Swinyard et al. 2008) mission. It will offer the large FoV and high spectral resolution required to break the confusion limit using spectroscopy. According to its current specifications SPICA will have a 3.5 m diameter mirror, and therefore will be subject to the same confusion noise as Herschel. The primary mirror will, however, be cooled to  $<6$  K and so will offer a great leap in sensitivity over Herschel. SAFARI will cover the waveband 35 to 210  $\mu\text{m}$  with varying resolution, including  $R \sim 1000$  - (at 120  $\mu\text{m}$ ,  $\Delta\lambda = 0.176 \mu\text{m}$ , when run in SAFARI’s higher resolution mode) - which matches the typical width of an extragalactic MIR/FIR emission line.

Estimates of source redshift were made by hand by locating the position of the strongest emission line in each spectrum. The strongest lines typically observed in the FIR are the [OI] and [CII] lines at 63.18 and 157.74  $\mu\text{m}$  respectively. If one assumes a typical dust temperature of 35 K, then the strongest lines shortward and longward of the peak of the SED will be [OI] and [CII] respectively. Beyond  $z = 2.5$  these lines are shifted out of SAFARI’s observable waveband, therefore the redshifts of more distant sources than this are irretrievable. If these two lines were the only ones present in the FIR then by comparing the evaluated source redshifts with the model input redshifts, one can assess the efficiency of this blind-line method. It was found that when looking at a patch of simulated ‘sky’ equal to one SAFARI FoV, it was possible to retrieve accurate redshifts for sources with 120  $\mu\text{m}$  continuum fluxes as much as a factor of  $\sim 10$  below the traditional continuum confusion limit. Sources with 120  $\mu\text{m}$  flux  $S_{120\mu\text{m}} > 1$  mJy and at redshifts  $z < 2.5$  were retrieved with 100% accuracy.

The use of blind spectral line surveys to resolve FIR sources is not without its own limitations and type of confusion. Line, or spectral confusion occurs when multiple sources are observed in a single telescope beam: the spectra from two or more objects are effectively scrambled, and it can become difficult to determine which lines are emitted by which objects. As a result, source redshifts become

hard to extract. The work described in Clements et al. (2007) made use of model spectra with FIR emission lines only. To assess the true viability of using spectral line surveys to break the confusion limit requires the inclusion of MIR emission lines in the ‘sky’ model, as sources will, in general, have both FIR and MIR emission lines. Inclusion of these shorter wavelength lines will enable the recovery of sources with redshifts of  $z > 2.5$ , beyond which the [OI] and [CII] emission lines at 63.18 and 157.74  $\mu\text{m}$ , respectively, are shifted out of the SAFARI waveband. By including MIR lines however, one increases the problem of line confusion, and so assigning lines to individual, but spatially unresolved, sources becomes more problematic.

In this paper we examine a much larger model ‘sky’ populated with more realistic template spectra with both FIR and MIR emission lines and employ a new automated method of evaluating source redshifts in a time efficient manner. We also implement a method to extract the redshifts of multiple sources clustered in a single spatial bin. Through the implementation of this method we investigate how effectively we can break the traditional photometric confusion limit. In sections 2.1 and 2.2 we describe the generation of the artificial sky used to test the source recovery technique, which in turn is outlined in section 2.3. This is followed in section 3 by a quantitative assessment of the retrieval and error rates of the redshifts output, and a discussion of the results in section 4.

## 2. Extracting Redshifts From an Artificial Sky

Deep, blind-field imaging spectroscopy has the potential to enable discrete sources at fluxes below the traditional continuum confusion limit to be extracted. Using imaging spectroscopy, it is theoretically possible to extract redshifts for all line emitting sources present in the instrument’s FoV, allowing all sources to be discretely resolved. In this work this is done using an automated redshift determination algorithm. In order to best test the efficiency (number of sources for which we determine redshifts, inversely weighted by how many sources we inaccurately determine redshifts for) of this method we generate an artificial sky in the form of a datacube, populated with realistic spectra taken from nearby galaxies, and redshifted according to the bright-end and burst mode galaxy evolution models of Pearson (2005), Pearson et al. (2007) and Pearson & Khan (2009). Running the program through the datacube we compare the fitted redshifts with their input values in order to determine the method’s precision, accuracy and efficiency.

### 2.1. Generating an Artificial Sky

We create an initial set of two 1 square degree artificial skies with 1” spatial pixels, populated by galaxies with redshifts, spectral types and 40  $\mu\text{m}$  continuum fluxes based on the bright-end and burst mode evolutionary models of Pearson (2005), Pearson et al. (2007) and Pearson & Khan (2009). We do not include any physically based spatial distribution modelling (eg. clustering, etc.) and in this work the skies are populated with sources

uniformly distributed in random positions. It should also be noted that we do not include any cirrus contribution and we assume SAFARI to be background limited. These act as our master 'skies' which we later crop and re-bin to create the SAFARI footprints.

The bright-end and burst mode evolutionary models are backward evolution formulations where observed galaxy source counts are used to constrain the model parameters. The model components consist of a luminosity function to represent the number density of sources as a function of luminosity, a library of spectral energy distributions (SED) to model the extragalactic source population emission as a function of wavelength and an assumption on the type-dependent evolution of the extragalactic population (in luminosity and number density). Both evolutionary models utilize the IRAS infrared local luminosity function defined at  $60\mu\text{m}$  (Saunders et al. 2000) or  $12\mu\text{m}$  (Rush et al. 1993) for the galaxy and AGN (Seyfert) populations respectively. Although various other, more recent luminosity functions are available, the IRAS functions has the advantage of being defined at or around the peak of the population emission spectrum and are free of contamination by mid-infrared features. The  $60\mu\text{m}$  galaxy luminosity function is segregated into cool (normal galaxy) and warm (star-forming) components, defined by IRAS colours where cool  $100\mu\text{m}/60\mu\text{m}$  cirrus-like colours (Efstathiou & Rowan-Robinson 2003) represent the normal quiescent galaxy population and the warmer  $100\mu\text{m}/60\mu\text{m}$  colour component is representative of star-forming galaxies with activity increasing as a function of luminosity for M82-like Starburst  $L_{IR} < 10^{11}L_{\odot}$ , luminous (LIRG)  $L_{IR} > 10^{11}L_{\odot}$  & ultraluminous (ULIRG)  $L_{IR} > 10^{12}L_{\odot}$  infrared galaxies. Thus the model framework includes five general evolutionary population classes (Normal, Starburst, LIRG, ULIRG, AGN) of extragalactic object defined by luminosity, colour and subsequent evolution.

The bright-end model assumes evolution in the galaxy population in both the density and luminosity for sources modeled by simple power laws of the form  $f(z) = (1+z)^k$ , where  $k$  is the type dependent evolutionary strength parameter. The evolutionary model is an updated framework of that first presented in Pearson & Rowan-Robinson (1996), with modest starburst galaxies rather than ULIRGs dominating in  $15\mu\text{m}$  selected source counts. The burst mode evolutionary model predicts that the upturn of emission at  $15\mu\text{m}$  (Elbaz et al. 1999) and peak at  $24\mu\text{m}$  (Papovich et al. 2004) is due the emergence of a new population of L/ULIRGs. The original burst mode evolutionary model presented by Pearson (2001) has power law evolution similar to the bright-end model for the starburst and AGN sources and an initial violent exponential evolutionary phase of the form,  $f(z) = 1 + f.exp[-\frac{(z-z_p)^2}{2\sigma^2}]$ , from  $z = 0$  to  $z_p = 1$ , where where  $k$  &  $\sigma$  are the type dependent evolutionary strength parameters, followed by a power law evolutionary phase for the L/ULIRGs. Both the bright-end and burst mode evolutionary models have non-evolving nor-

mal galaxy populations. Throughout this work, values regarding the different evolution models are written in the form bright-end(burst mode).

Each of the five general evolutionary population components (Normal, Starburst, LIRG, ULIRG, AGN) are represented by a small set of galaxy spectral energy distributions from the libraries of Efstathiou & Rowan-Robinson (2003), Efstathiou et al. (2000) and Efstathiou & Rowan-Robinson (1995) for the normal, starburst, L/ULIRG and AGN types respectively. The selected SEDs are representative of the SED libraries from which they have been drawn and have been shown to be consistent with the colours of sources detected in the European Large Area ISO Survey (Oliver et al. 2000). Rowan-Robinson et al. (2004) showed that the ISO infrared galaxy population could indeed be divided into four general spectral classes; normal quiescent galaxies; starburst (M82-like) galaxies; luminous and ultraluminous infrared galaxies and AGN. Rowan-Robinson et al. (2004) found that the normal, quiescent population of ISO galaxies were well modelled with the templates of Efstathiou & Rowan-Robinson (2003) with far/mid-infrared ratios of  $\nu S_{\nu}(100\mu\text{m})/\nu S_{\nu}(12\mu\text{m}) \sim 6-7$  whilst in contrast, IRAS galaxies were often modelled with templates with ratios of  $\sim 5$  (Rowan-Robinson & Crawford 1989). Therefore, the normal galaxy component consist of 2 SEDs each of  $\nu S_{\nu}(100\mu\text{m})/\nu S_{\nu}(12\mu\text{m}) \sim 5.8$  &  $6$  referred to as a normal and cold normal type respectively. For the star forming (starburst, L/ULIRG) population we have selected 7 SEDs from the template libraries to ensure a variation in the the mid-infrared features in an attempt to avoid artifacts caused by a particular choice of SED for all sources. The SEDs in the template libraries have a broad correlation between the model optical depth and the galaxy luminosity. 2/7 of these SEDs are selected for the starburst component ( $\tau_V \sim 50$  of which one is a model for the archetypal star-forming galaxy M82). 3/7 of these SEDs are selected with increasing optical depths ( $\tau_V \sim 50 - 100$ ) for the LIRG component (assuming a corresponding increase in luminosity for each SED of  $10^{11}L_{\odot}$ ,  $10^{11.5}L_{\odot}$  and a colder SED of  $L > 10^{11.5}L_{\odot}$  referred to as a cold-LIRG) and the remaining 2/7 SEDs selected for the ULIRG component correspond to the best template model fits for the archetypal ULIRGs Arp220 (cold ULIRG) and Mk231 (hot ULIRG) respectively. Given the relatively featureless infrared spectra of AGN, the AGN component SED corresponds to a single tapered disc dust torus model. Emission lines are then added to each of the template spectra, taken from ISO-LWS observations of nearby galaxies (eg. Negishi et al. 2001).

MIR emission line strengths are taken, where possible, from the same sources as are used for the FIR emission lines. In some cases data were not currently available at these shorter wavelengths in which case sources with similar FIR characteristics as the original template spectra are used. The galaxies from which we take the MIR emission line strengths are listed in table 1. The model spectra are shown in figure 1 and are added to the master 'sky' in spectral resolution of  $\Delta\lambda = 0.08\mu\text{m}$  ( $R = 2500$  at  $200$

Component	Galaxy Type	Line Template	Reference
Normal	Cold/Normal	NGC 7331	Smith et al. 2004
Starburst	M82/Starburst	M82	Förster Schreiber et al. 2001
LIRG	$10^{11/11.5} L_{\odot}$ /Cold LIRG	NGC 253	Sturm et al. 2000
ULIRG	Hot/Cold ULIRG	Arp 220	Sturm et al. 1996
AGN	Seyfert 1	Mrk 1014	Armus et al. 2004
AGN	Seyfert 2	NGC 1068	Lutz et al. 2000

**Table 1.** Sources used for the addition of MIR lines to the template spectra that populate the data cube.

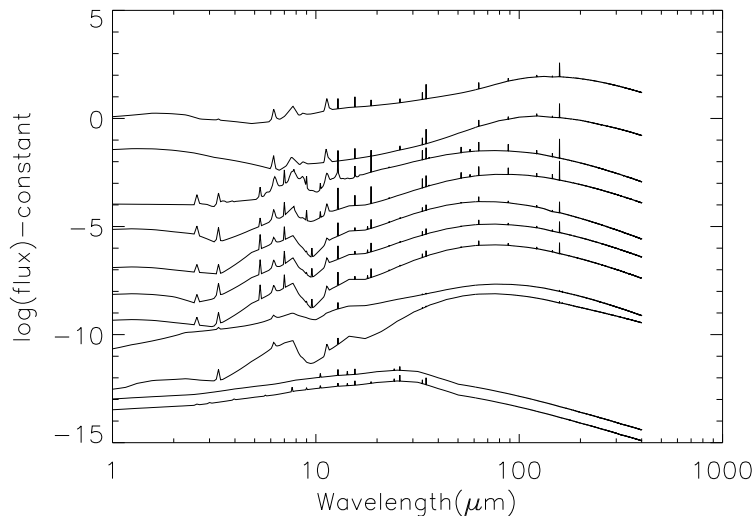


**Fig. 1.** Template spectra which were used to populate the datacube. From the top downwards are the SED templates for; normal cold, normal, starburst M82, starburst,  $10^{11} L_{\odot}$  LIRG,  $10^{11.5} L_{\odot}$  LIRG, cold LIRG, hot ULIRG, cold ULIRG, Seyfert 1 and Seyfert 2.

$\mu\text{m}$ ) in the waveband from 1 to 400  $\mu\text{m}$ .

The flux and redshift distributions for each SED type for the bright-end and burst mode evolution models are shown in figure 2. These figures show the distribution of SED type with 120  $\mu\text{m}$  flux and redshift over a 1 square degree region of sky. In these regions of sky there are a total of 25596(38975) sources with  $S_{120\mu\text{m}} > 0.342$  mJy ( $1\sigma$ , 10hr sensitivity of SAFARI). Of these sources 33(58)% have  $S_{120\mu\text{m}} > 1$  mJy. The burst mode evolution model includes more high flux sources as well as more high redshift sources than the bright-end model. The burst mode model also includes the more extreme luminous/ultraluminous and Seyfert spectral types, which tend to dominate at higher redshifts. 100(75)% of sources with  $S_{120\mu\text{m}} > 1$  mJy have redshifts  $z < 2.5$ , however setting  $S_{120\mu\text{m}} > 0.342$  mJy these values drop to 95(74)%.

## 2.2. Generating Datacubes/Source Catalogs

SAFARI (Swinyard et al. 2008) will have a  $2' \times 2'$  FoV with a diffraction-limited angular resolution of  $8''$  at 120  $\mu\text{m}$ . The instrument will cover the waveband from 35 to 210  $\mu\text{m}$  at varying spectral resolution ( $R \sim 1000$  at 120  $\mu\text{m}$ ). However, in this work we match our data cubes to the original specifications of SAFARI, taking a FoV of  $128'' \times 128''$  and a waveband covering from 30 to 210  $\mu\text{m}$ . Thus to generate datacubes representative of the sky as

would be seen by SAFARI we take  $128'' \times 128''$  sections of our artificial skies and re-bin to a spatial resolution of  $8''$  (to simplify we have assumed a wavelength independent spatial and spectral resolution). This re-binning allows for the possibility of two or more sources in a single spatial bin. In these cases we refer to the brightest source with  $S_{120\mu\text{m}} > 0.342$  mJy as the primary source and the second brightest  $S_{120\mu\text{m}} > 0.342$  mJy as the secondary source. Applying the angular resolution of SPICA means that 6(8)% of all pixels have two or more sources present. If there are multiple sources present in a spatial pixel only the two brightest will be investigated as other sources will be too faint relative to the primary and secondary sources to detect. We create our spectra by cropping the waveband of the artificial sky to between 30 and 210  $\mu\text{m}$  with and smoothing them to a fixed resolution of  $\Delta\lambda = 0.176 \mu\text{m}$ . In this work we use the original wavelength range SAFARI rather than its current specification, thus we have a slightly larger waveband to pick up emission lines from. We then add Gaussian noise with a standard deviation of  $\sigma = 0.342$  mJy and a zero mean along each spectrum<sup>1</sup>. A datacube representing a single SAFARI footprint will therefore be  $16 \times 16 \times 1024$  pixels in size.

<sup>1</sup> This is the noise commensurate with the sensitivity of SAFARI for a 10hr integration time.

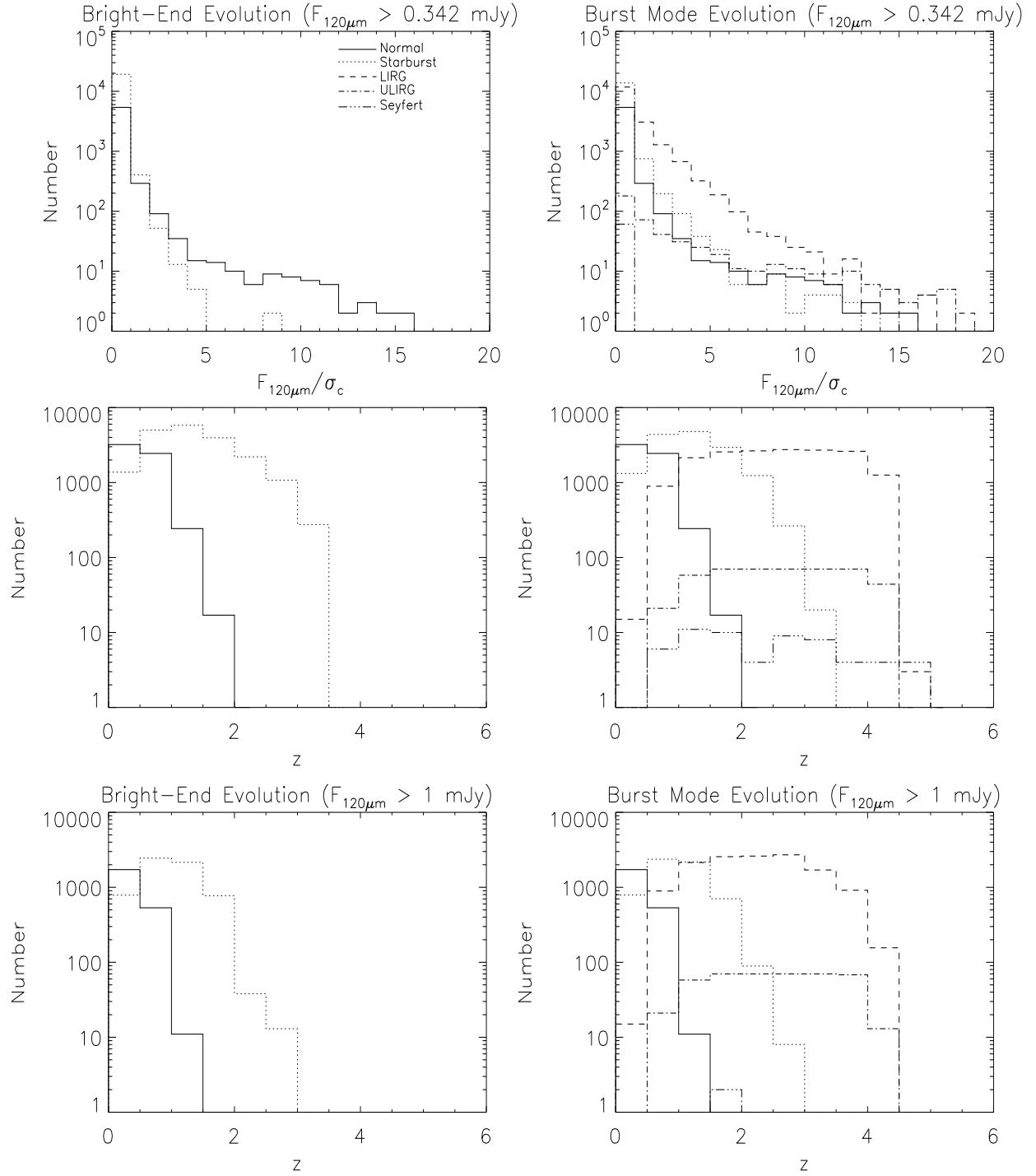


**Fig. 2.** A plot of the flux (top row) and redshift (bottom two rows) distributions, for each SED type, of the sources that populate the bright-end and burst mode evolution data cubes respectively. The top two rows are for sources with  $120 \mu\text{m}$  flux,  $S_{120\mu\text{m}} > 0.342 \text{ mJy}$  and the bottom row is for sources with  $S_{120\mu\text{m}} > 1 \text{ mJy}$ . Values are for a 1 square degree region of sky. Flux is measured as a fraction of the  $120 \mu\text{m}$  confusion limit,  $\sigma_c = 4.3 \text{ mJy}$

A ‘truth’ catalog is simultaneously generated which tracks the location of each source in a datacube, as well as the redshift, SED type and  $120 \mu\text{m}$  flux. This allows a later comparison between retrieved and input redshifts after we apply our redshift determination algorithm. This is the same datacube and ‘truth’ catalog generation method as used by Clements et al. (2007).

Datacubes are generated for both burst mode and bright-end evolutionary models. For each evolutionary model 100 different datacubes are investigated (i.e. taken from different regions of the larger 1 square degree cube) in order to account for variance in the random spatial distributions, each of a size equivalent to 1 SAFARI FoV (i.e. a total area of  $2' \times 2'$ ). For each cube the noise along the spectra is added by creating 10 differently seeded randomly generated Gaussian noise arrays in order to account for the variance of results due to noise. We therefore have a total of 1000 datacubes for each evolutionary model. By way of comparison, a figure of  $\sigma_c(\lambda = 120 \mu\text{m}) = 4.3 \text{ mJy}$  is adopted for the confusion limit, based on Dole et al. (2004).

### 2.3. Detecting Sources and Extracting Their Redshifts

Redshifts are determined using a pseudo-cross-correlation (PCC) method and stored - however, first the presence of a source must be confirmed. This is done by checking the  $120 \mu\text{m}$  flux,  $S_{120\mu\text{m}}$ , of each spatial pixel in the cube against a limiting value. This action is performed before any other operations take place, thereby saving processing time on analyzing non-existent or too-faint sources. We assume that if any spatial pixel has  $S_{120\mu\text{m}} > 0.342 \text{ mJy}$  (which is equivalent to the  $1\sigma$  noise in a single spectral pixel for 10 hours of integration) then a source is present and we attempt to determine its redshift. This value was chosen as our continuum cutoff value as empirically it is found that if a source has  $120 \mu\text{m}$  flux less than this then typically the emission lines are too faint to reliably use with our method. A flow diagram illustrating the sequence of this method is shown in figure 3.

Each spectrum is preprocessed prior to redshift determination in the following way: a) Each spectrum is fit with a fourth order polynomial which is taken to represent the continuum emission of the source; b) the  $S_{120\mu\text{m}}$  value of the spectrum is checked against a limiting value: if  $S_{120\mu\text{m}} <$  the limiting value, the source is considered too faint to determine its redshift, and no further analysis is conducted on the spectrum; c) The polynomial continuum fit is subtracted from the spectrum, leaving an array containing only emission lines and noise (see figure 4)

The spectral channels in the aforementioned array containing the 6 highest continuum subtracted flux levels (with  $S_\lambda > 2\sigma$ ) are then initially considered to be emission lines and are taken to be our observed lines in our observed line array ( $OLA$ ). Empirically it is found that if the ratio of the strongest to weakest (continuum subtracted) line fluxes present in  $OLA$  is less than 1.5 then these lines most likely arise from noise and we therefore consider such an array to contain no genuine emission lines. Further analysis is only conducted on spectra with higher ratio values

than this.

$OLA$  is 1024 spectral channels in extent (i.e. identical to the spectral extent of our data cube), and contains the continuum-subtracted flux of our 6 observed possible emission lines at the appropriate spectral channels corresponding to the wavelengths of those lines, and zero elsewhere. In the case of an emission line stretching across multiple pixels, the line is compressed into a single channel and there is a built in tolerance in the redshift fitting routine to allow for this. The brightest channel present in  $OLA$  is assumed to hold a genuine emission line. The wavelength of this emission line is then compared to the set of template wavelengths compiled from a list of the strongest emission lines typically seen in galactic spectra in the MIR/FIR. This template line array ( $TLA$ ) is equal to one at the appropriate spectral channels corresponding to the wavelengths of the template emission lines, and zero elsewhere. This comparison then provides a table of possible redshifts the source may lie at.

If the strongest line in  $OLA$  lies at  $\lambda_{brightest}$ , and our template emission lines lie at wavelengths  $\lambda_{template_j}$ , where  $j$  is the indexing of the line in our template (eg. for [OIII]@51.82  $\mu\text{m}$   $j = 1$ , for [NIII]@57.32  $\mu\text{m}$   $j = 2$  etc.), then an array of possible redshifts at which the source may lie can be determined from:

$$z_k = \frac{\lambda_{brightest}}{\lambda_{template_j}} - 1 \quad (1)$$

Where  $k = 1, 2, \dots, l$ , where  $l$  is the total number of lines in  $TLA$  and thus the total number of possible redshifts. The array of template emission lines,  $TLA$ , which was used to determine the set of possible redshifts is now also used to fit to the observed possible emission lines,  $OLA$ . Thus in order to find the redshift at which  $TLA$  most closely correlates to  $OLA$ ,  $TLA$  is shifted to each of the possible source redshifts, as in;

$$\lambda_{template_{jk}} = \lambda_{template_j}(1 + z_k) \quad (2)$$

We now have  $l$  binary redshifted template line arrays ( $TLA_k$ ), each of which are 1024 spectral channels in extent and are defined by;

$$(TLA)_{ik}(\lambda_i = \lambda_{template_{jk}}) = 1 \quad (3)$$

$$(TLA)_{ik}(\lambda_i \neq \lambda_{template_{jk}}) = 0 \quad (4)$$

where  $i$  is the spectral channel corresponding to a given wavelength. The strength of the correlation between our observed line array and each template line array is given by;

$$C_k = \sum_{i=0}^{i=1023} (OLA)_i (TLA)_{ik} \quad (5)$$

The value of  $z_k$  which gives the highest value for  $C_k$  is then assigned as the best estimate of the source redshift. In this way the strength of the match depends both on the strength of the continuum subtracted emission lines that are coincident between the observed spectrum and the redshifted line templates, and the number of matches

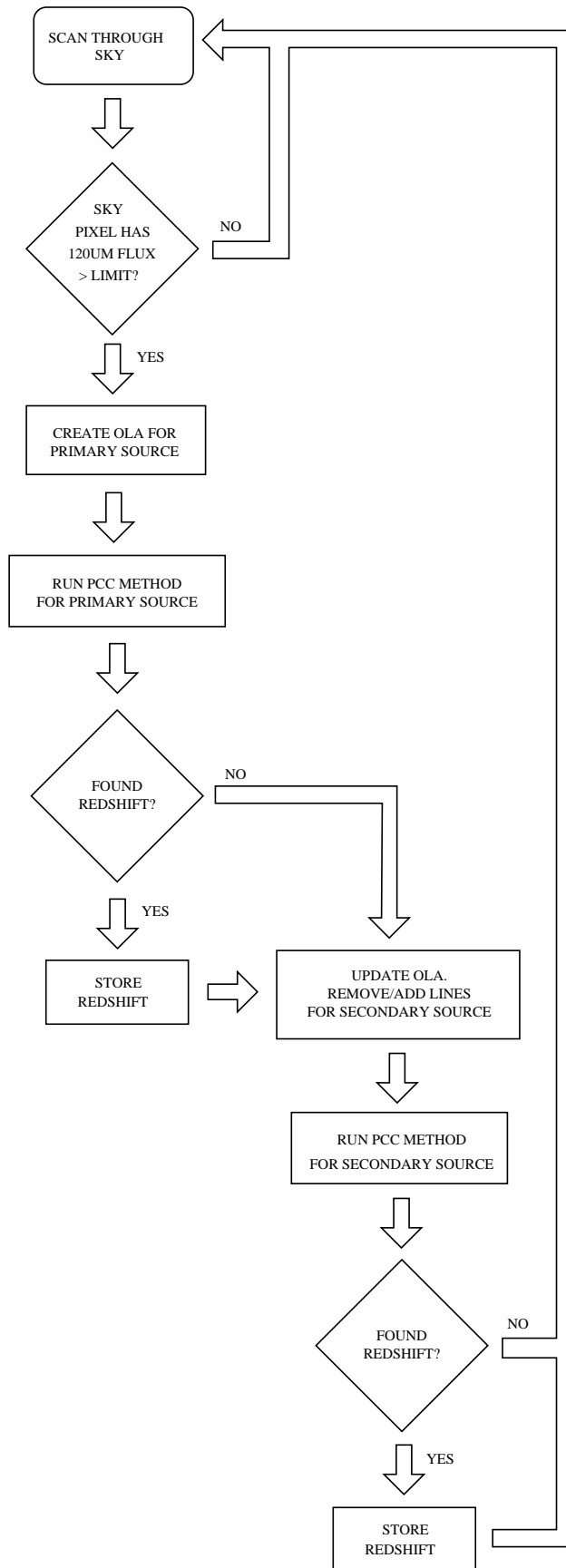
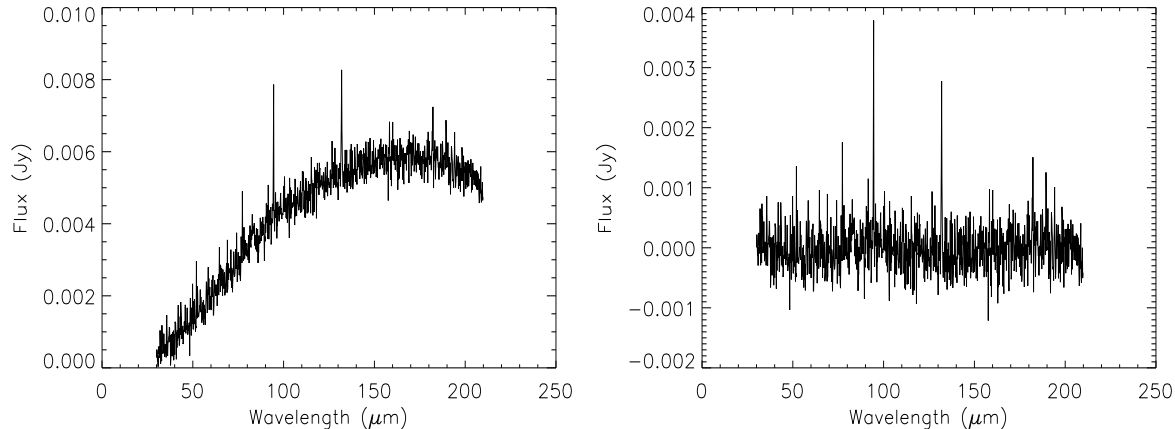


Fig. 3. A flowchart of the order in which the sources are observed and then our redshift determination method implemented.



**Fig. 4.** Shown in the left panel is a sample spectrum as can be found in our artificial ‘skies’. In our PCC redshift determination algorithm the continuum of this spectrum is fit with a fourth order polynomial. This fit is then subtracted from the spectrum, leaving an array containing only emission lines and noise. The right panel shows the example spectrum after the continuum fit has been subtracted.

between lines of the observed and template emission line arrays.

To improve the accuracy of our method, use is made of additional, a-priori information, and redshifts which produce template/observed array emission line matches for strong, commonly observed emission line pairs are weighted more heavily. The additional weighting values for  $C_k$  when a characteristic pair is found are determined empirically to give the most favorable ratio of accurate to inaccurate source redshift evaluations<sup>2 3</sup>. Eg. one of the strongest line combinations in the MIR is the [SIII]/[SiII] pair at rest wavelengths of 33.42 and 34.82  $\mu\text{m}$  respectively, both of which are found to be strong in starburst galaxies. If a match is made between the observed line array and this line pair, then  $C_k$  is weighted by an extra factor of 2. Two other, weaker, line combinations included in our template array are the [OIII]/[NIII] and [OIII]/[NII] pairs at rest wavelengths of 51.82, 57.32, 88.36 and 121.90  $\mu\text{m}$  respectively. If a match is made between the observed line array and either of these line pairs, then  $C_k$  is weighted by an extra factor of 1.5.

We include an additional criterion that, as the strengths of the members of the [OIII]/[NIII] and [OIII]/[NII] lines pairs are typically comparable, any value of  $z_k$  which gives a match in the observed line array with one member of either of these pairs, but not its partner, is rejected. This relationship holds for all the model spectra used in this work, however it may not always hold in practice when encountering genuine spectra as observed in extragalactic

surveys.

In contrast to the work described in Clements et al. (2007), we can no longer assume that the strongest emission line in the spectrum shortward of the continuum emission peak (determined from the position of the peak of the polynomial fit) is the [OI] line at 63.18  $\mu\text{m}$ , as we now have strong MIR lines present in the spectra. We can, however, still assume that the strongest line longward of the continuum emission peak is the [CII] line at 157.74  $\mu\text{m}$ . This is true as long as the reasonable assumption that  $T_{dust} \lesssim 20$  K holds, as [CII] is then typically the only strong line longward of the SED peak. Thus, if no single redshift is able to map the line template onto the observed line array, but the strongest line in the spectrum lies longward of the SED peak, and has a line to continuum ratio  $> 3$  (found empirically to be the lowest value to reliably use to identify the [CII] emission line at 157.74  $\mu\text{m}$  in this circumstance), we assume it to be the [CII] line and, from this, calculate a redshift.

An evaluated redshift is recorded along with the position of the source on the sky. The redshift is referred to as the primary redshift and is considered to be that of the brightest, or primary, source in the given spatial bin. A slightly modified redshift extraction algorithm is then run a second-time through the spectrum, to determine whether there is a second source of lower flux present; the secondary source. When attempting to extract a redshift for the secondary source in any spatial bin we first zero the lines in *OLA* which we have already associated with the primary source. We then add to *OLA* the 3 strongest lines in the spectrum that have not yet been used in redshift fitting to the spectrum, with flux  $S_\lambda > 3.5\sigma^4$ . This

<sup>2</sup> An evaluated source redshift is defined as being accurate if it differs from the input model redshift by less than 0.1, i.e.  $|z_{evaluated} - z_{catalog}| = \Delta z < 0.1$

<sup>3</sup> Taking as an example three different weighting values: *A*, *B* and *C*. *A* outputs 3 accurate redshifts and 0 inaccurate redshifts. *B* outputs 20 accurate redshifts and 10 inaccurate redshifts. *C* outputs 15 accurate redshifts and 3 inaccurate redshifts. Of these weighting values we would use *C* as this outputs a high number of accurate redshifts, while limiting the number of inaccurate redshifts.

<sup>4</sup> Eg. defining a line as any spectral channel which has  $S_\lambda > 2\sigma$ , if a spectrum contains 20 spectral channels with  $S_\lambda > 2\sigma$ , we populate *OLA* with the brightest 6 of these lines, leaving 14 unused lines in the spectrum. In order to determine a secondary redshift we zero the lines in the *OLA* which we have already associated with the primary source. If, for example, 4 lines in



line selection process is used as a) We find empirically that 6 is the optimum number of emission lines required to accurately fit a primary redshift (i.e. the maximum amount of lines the algorithm is able to use before encountering significant degeneracies) b) By definition the secondary source is fainter than the primary, thus we expect noise to be more of a significant hindrance in redshift fitting - therefore we need more stringent requirements on the strength of the emission lines used c) 3 is found to be the optimum number of lines to add to the previously selected lines which are not found to be associated with the primary source - if all 6 lines of the initially selected lines are found to be associated with the primary source then 3 emission lines is the minimum number that can be used to reliably fit a redshift and any more than this can result in significant degeneracies in redshift fitting. The algorithm now runs in a manner very similar to before, however (1) by definition we expect the continuum-subtracted emission lines from the secondary source to be of lower flux than those of the primary, and so the requirement on the ratio of the strongest to the weakest emission line in the observed array is dropped to 1.3, and (2) also by definition we are looking at sources of fainter continuum flux, and thus are more susceptible to picking up spurious emission lines: we therefore no longer weight more heavily redshifts which give matches for characteristic MIR/FIR emission line pairs, and no longer allow redshifts to be determined from the single [CII] emission line. Both these changes in the algorithm for secondary as opposed to primary redshift determination are implemented as empirically they are found to give the most reliable results.

The PCC method works by moving through each spectrum in the cube and cross-correlating MIR/FIR line templates at a discrete rather than continuous set of redshifts. This means that the number of discrete redshifts fitted is far less than the number of redshift steps required when fitting continuously over a given range. This means we are using less of the spectrum and thus are less likely to encounter a pixel with a high noise level which could be miss-identified as an emission line. We are therefore able to use weaker emission lines for redshift determination, which enables the algorithm to probe more deeply into the noise. This is particularly powerful when looking at secondary sources which typically will have weaker line fluxes than primary sources

### 2.3.1. FIR Emission Lines Only

As a first test of our automated redshift determination we compare how efficiently our method works in comparison to that described in Clements et al. (2007). Clements et al. made use of spectra containing FIR emission lines only, therefore a direct comparison of this original method, and our PCC method as described in section 2.3 can only

---

the *OLA* contributed to the highest value of  $C_k$  then these are zeroed, leaving 2 lines remaining in *OLA* which can be used to determine a secondary redshift. Of the 14 remaining unused lines above  $2\sigma$  in the spectrum, 10 of these for example may have fluxes  $S_\lambda > 3.5\sigma$ , the 3 brightest of which we add to *OLA*. The *OLA* used to attempt to determine a secondary redshift therefore contains a total of 5 lines.

be made when using exactly the same spectra. To do this we use a variant of our PCC method which uses FIR emission lines only. The lines are listed in table 2. In addition, only the [OIII]/[NIII] and [OIII]/[NII] pairs at 51.82/57.32 and 88.36/121.90  $\mu\text{m}$  respectively are used to additionally weight  $C_k$ , as these are the only characteristic pairs which lie in the FIR waveband as defined by Clements et al.

### 2.3.2. MIR and FIR Emission Lines

The general version of our method by default uses both MIR and FIR lines in our template array, which are listed in table 3. The version of the method also allows us to make use of all of our characteristic emission line pairs.

## 3. Results

All results given in this section were determined by taking the averaged values for each of 100 FoVs ( $\times 10$  differently seeded noise arrays) for both bright-end and burst mode evolution. When quoting results from this work we give the number of accurate redshifts retrieved as a percentage of the total number of sources within a given flux and redshift range in the datacube. However the number of inaccurate redshifts are given as a percentage of the total number of redshifts output by the algorithm under the same constraints<sup>5</sup>.

### 3.1. Results From Method of Clements et al. (2007)

The work described in Clements et al. (2007) made use of spectra containing FIR emission lines only, and results were only determined for the burst mode evolution model. They found that all sources with redshifts at  $z \leq 2.5$  with  $S_{120\mu\text{m}} \geq 1$  mJy could be retrieved. Redshifts higher than this could not be determined, as beyond  $z = 2.5$  the [OI] and [CII] lines are redshifted out of the SAFARI passband. Lower flux sources, as much as  $\sim 10$  times fainter than the traditional continuum confusion limit were also retrieved, albeit with lower efficiency.

### 3.2. Analysis Using FIR Emission Lines Only

#### 3.2.1. Primary Sources

Using the FIR emission line only version of the method outlined in section 2.3.1 we find that we recover accurate redshifts for 85(46)% of all primary sources with  $S_{120\mu\text{m}} \geq 1$  mJy, with 5(10)% of all primary redshifts output by the algorithm under the same constraints being inaccurate. The aforementioned recovery values are given as a percentage of all sources, including those at  $z > 2.5$ , however by definition this method is unable to retrieve redshifts for sources at  $z > 2.5$ . Beyond  $z = 2.5$  the redshift recovery rate drops to zero for both evolutionary models. For sources with  $S_{120\mu\text{m}} \geq 1$  mJy lying at  $z < 2.5$  the recovery of redshifts for primary sources is  $\sim 85(64)\%$ . Under the same constraints Clements et al. (2007) retrieved ac-

---

<sup>5</sup> Eg. a datacube has 100 sources within the specified redshift and flux range and the algorithm outputs 50 redshifts; 40 accurate and 10 inaccurate. The results statement would then be given in the following form; we retrieve 40% of sources in our flux and redshift range accurately, with 20% of redshifts output by the algorithm under the same constraints being inaccurate.

Emission Line	OIII	NIII	OI	OIII	NII	OI	CII
Wavelength ( $\mu\text{m}$ )	51.82	57.32	63.18	88.36	121.90	145.53	157.74

**Table 2.** Lines used in source redshift determination through template fitting for the FIR emission line only method.

Emission Line	NeII	SIII	SIII	SiII	OIII	NIII	OI	OIII	NII	OI	CII
Wavelength ( $\mu\text{m}$ )	12.81	18.71	33.42	34.82	51.82	57.32	63.18	88.36	121.90	145.53	157.74

**Table 3.** Lines used in source redshift determination through template fitting for the method using both FIR and MIR emission lines.

curate redshifts for 100% of the sources. However in that work redshifts were determined manually for each source whereas in this work they are determined automatically. Unlike Clements et al. we are unable to assess each spectrum on a case by case basis. Therefore in attempting to minimize the number of incorrect redshifts output by the algorithm we are forced to limit the maximum possible efficiency of the accurate redshift recovery of the algorithm.

By dropping our 120  $\mu\text{m}$  flux cutoff to  $S_{120\mu\text{m}} \geq 0.342$  mJy, we find that we recover accurate redshifts for 36(33)% of all primary sources with  $S_{120\mu\text{m}} \geq 0.342$  mJy, with 12(13)% of all redshifts output by the algorithm under the same constraints being inaccurate. Taking into account only sources at  $z < 2.5$  our accurate recovery becomes 45(39)%. Despite this being a lower recovery percentage than for  $S_{120\mu\text{m}} \geq 1$  mJy the majority of sources have lower fluxes than this. As such by dropping the cutoff flux from 1 mJy to 0.342 mJy we have increased the total number of accurate redshifts recovered by 22(15)%.

### 3.2.2. Secondary Sources

Using our FIR emission line only PCC method we retrieve accurate redshifts for  $\sim 30(27)\%$  of all secondary sources when using a flux cutoff of  $S_{120\mu\text{m}} > 0.342$  mJy with  $\sim 6(4)\%$  of all secondary redshifts output by the algorithm under the same constraints being inaccurate.

### 3.3. Extending Analysis to MIR

By default, the full version of our PCC redshift determination method uses both MIR and FIR emission lines, and is that version which would be applied to real data. It is now possible to investigate sources at redshifts  $z > 2.5$  which account for 5(26)% of the population with  $S_{120\mu\text{m}} > 0.342$  mJy, of the evolutionary models. Accurate redshifts are retrieved for  $\sim 75\%$  of primary sources with  $S_{120\mu\text{m}} \geq 1$  mJy, for both bright-end and burst mode evolution, with respectively 6(8)% of all primary redshifts output by the algorithm under the same constraints being inaccurate. We see here that using both MIR and FIR emission lines is less efficient in recovering accurate redshifts than using FIR emission lines only at redshifts  $z < 2.5$ . This is due to the fact the ability to resolve redshifts  $z > 2.5$  is not as advantageous here as most sources with  $S_{120\mu\text{m}} \geq 1$  mJy lie at redshifts  $z < 2.5$  in both evolution models, however we are still subject to the disadvantage of significantly more degeneracies in redshift fitting due to a higher number of emission lines. Dropping the 120  $\mu\text{m}$  flux cutoff, 38(54)% of all primary sources with  $S_{120\mu\text{m}} \geq 0.342$  mJy are retrieved (see figure 5), with 14(9)% of all redshifts output by the algorithm under the

same constraints being inaccurate.

#### 3.3.1. Secondary Sources

Employing a 120  $\mu\text{m}$  cutoff of 0.342 mJy, we find that we are able to determine accurate redshifts for  $\sim 38(29)\%$  of secondary sources with  $S_{120\mu\text{m}} \geq 0.342$  mJy (see figure 6), with 11(18)% of all redshifts output by the algorithm under the same constraints being inaccurate.

## 4. Discussion

We find that using the PCC method as described in this work, we can recover redshifts for sources as much as 10 times below the traditional continuum confusion limit. We also find we are able to successfully retrieve redshifts from line confused spectra caused by multiple sources separated by smaller scales than the size of the beam on the sky. However, using the burst mode and bright-end evolutionary models of Pearson (2005), Pearson et al. (2007) and Pearson & Khan (2009), we find no spatial bins containing more than two sources with  $S_{120\mu\text{m}} \geq 0.342$  mJy and therefore we do not test whether or not our method would be able to disentangle more sources than this.

Shown in figure 7 is the cumulative recovery (fraction of sources accurately recovered with  $S_{120\mu\text{m}}$  less than that defined by the x-axis) efficiency with increasing flux. All source populations (the primary and secondary sources of both bright-end and burst mode evolution) have a strongly increasing cumulative recovery fraction at low fluxes which then levels off at fluxes higher than the confusion limit. This is because the bulk of their populations lie at fluxes fainter than the confusion limit.

The bright-end evolution model has a larger fraction of low flux sources, whereas the burst mode evolution model has a similar population of low flux sources, but also a larger number of brighter sources. The efficiency of our method falls off with decreasing flux (as illustrated in figure 5), therefore we retrieve the redshifts for the burst mode evolution model more efficiently than for the bright-end evolution model.

At higher fluxes the redshift determination efficiency for all populations goes to 100%, however at these higher fluxes there are relatively fewer sources. Even at 10% of the confusion limit, we are still retrieving redshifts for  $\sim 10\%$  of sources, and given that the number of sources at these fluxes is so large we are gaining information about a significantly larger number of galaxies than would be the case if we were confusion limited.

The percentage of retrieved redshifts which are in error is higher for secondary sources than for the primary

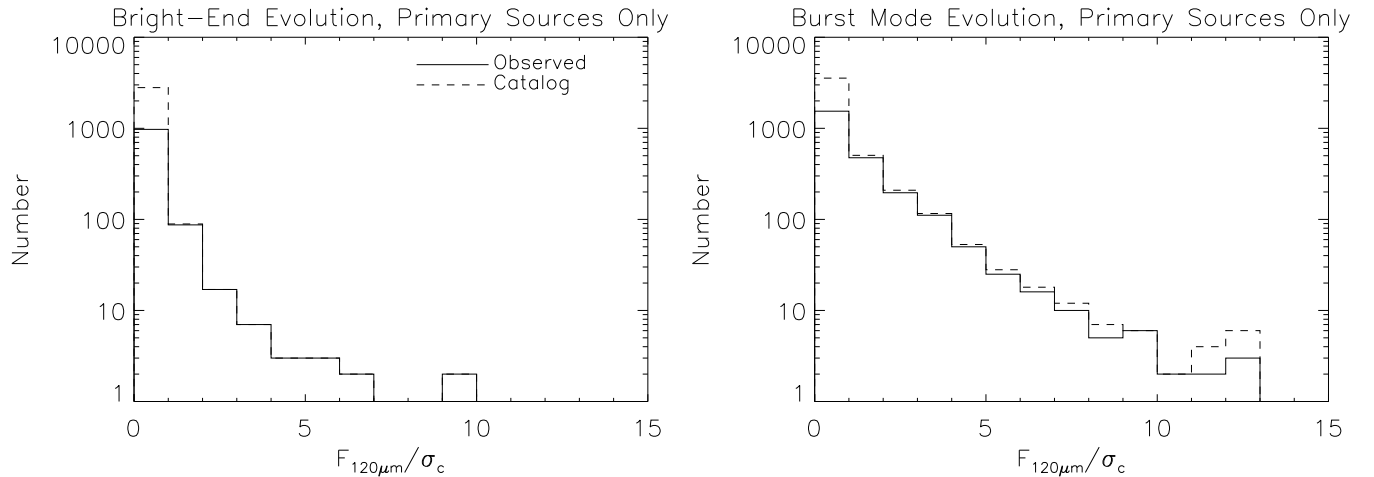


**Fig. 5.** Plots of the  $120 \mu\text{m}$  continuum flux distribution (with flux measured as a fraction of the  $120 \mu\text{m}$  continuum confusion limit,  $\sigma_c(\lambda = 120\mu\text{m}) = 4.3 \text{ mJy}$ ) for both the total input primary sources (dashed) and primary sources with accurately determined redshifts (solid). Shown in the left and right hand panels are the results for the bright-end and burst mode evolution models respectively. Results are for 100 SAFARI FoVs.

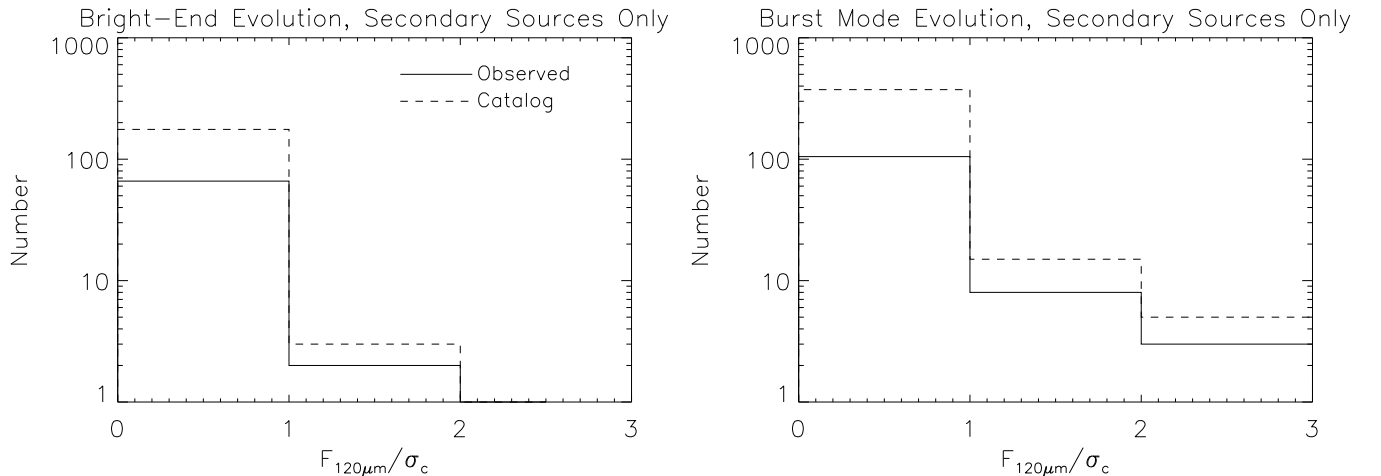


**Fig. 6.** Plots of the  $120 \mu\text{m}$  continuum flux distribution (with flux measured as a fraction of the  $120 \mu\text{m}$  continuum confusion limit,  $\sigma_c(\lambda = 120\mu\text{m}) = 4.3 \text{ mJy}$ ) for both the total input secondary sources (dashed) and secondary sources with accurately determined redshifts (solid). Shown in the left and right hand panels are the results for the bright-end and burst mode evolution models respectively. Results are for 100 SAFARI FoVs.

sources. This is to be expected because by definition the secondary sources are fainter than the primary. We are thus more likely to confuse noise with genuine emission lines. Another difficulty encountered when attempting to retrieve secondary redshifts is that we are unable to set a continuum flux limit to consider the source to be viable. Therefore we are most often attempting to retrieve redshifts from either very low flux or non-existent secondary galaxies, significantly increasing the likelihood of retrieving an erroneous redshift. This problem is lessened somewhat by the introduction of more stringent criteria in other areas when attempting to retrieve secondary redshifts, but it remains the cause of a large percentage of the inaccurate secondary redshift recoveries.

We find that by employing a cross correlation method for redshift determination, where we are only considering a very discrete set of redshift possibilities, we are able

to reduce the  $S_{120\mu\text{m}}$  cutoff value without drastically decreasing the efficiency of the method and thus are able to dig deeper into the instrumental noise. Employing the full MIR and FIR emission lines version of our method we find that we can retrieve accurate redshifts for a total of 38(52)% of all (i.e. both the primary and secondary sources) sources with  $S_{120\mu\text{m}} \geq 0.342 \text{ mJy}$  for bright-end and burst mode evolution respectively. Their respective frequency of occurrence of inaccurate redshifts as a percentage of all redshifts output by the algorithm under the same constraints is 15(10)%.

A limitation of this method is the possibility of sources with anomalous line strengths which can, for example, result in a miss-identification of the [CII] line. The possibility of such occurrences has not been taken in to account here. Further improvement to our PCC method would aim to decrease the total number of erroneous redshifts

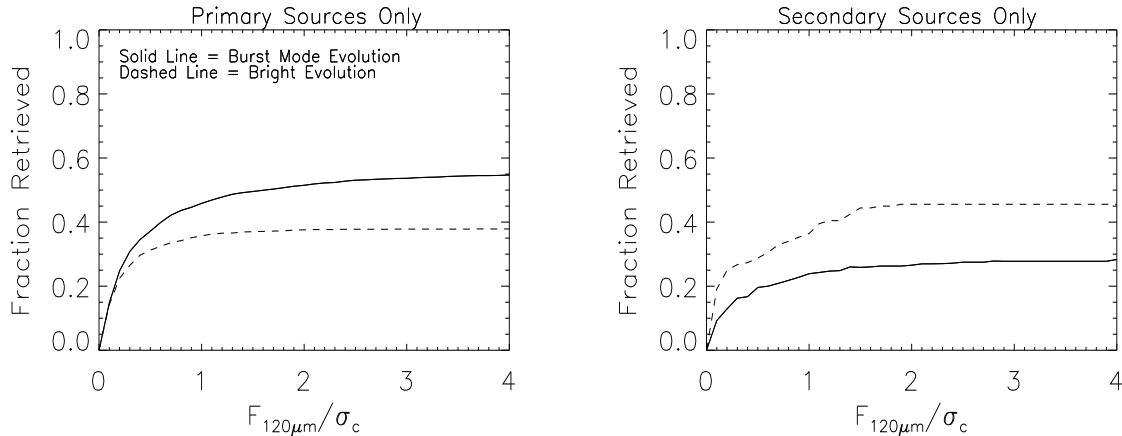


**Fig. 7.** Plots of the cumulative fractional recovery of sources (fraction of sources accurately recovered with  $S_{120\mu m}$  less than that defined by the x-axis) with increasing 120  $\mu m$  flux, measured as a fraction of the traditional 120  $\mu m$  continuum confusion limit,  $\sigma_c(\lambda = 120\mu m) = 4.3$  mJy. The left panel shows our results for primary sources and the right panel shows our results for secondary sources. The results for burst mode evolution are plotted as a solid line, and for bright-end evolution as a dashed line.

output for reasons such as this.

Additional spectral features that can be used for finding redshift are those associated with the PAHs (Polycyclic Aromatic Hydrocarbons). These features are much broader than the emission lines we have been using, thus observations could be made at lower spectral resolution, with a corresponding increase in instrument sensitivity. In this work we have modeled angular resolution as being constant over the full SAFARI band. If we were to employ a more realistic model for angular resolution we may observe sources which are clustered in a single spatial bin in our current 8" binning, as being separable (visible in different spatial bins) at shorter wavelengths. This could significantly decrease the fraction of erroneous redshifts output for secondary sources.

As discussed earlier, the sources from the bright-end evolution model are mostly at low fluxes whereas the burst mode has in addition a smaller population of high flux sources. This accounts for the difference in our recovery rates for the two models. It is therefore important to further test the efficacy of our technique, and of this deep observing mode of SAFARI spectral imaging on a number of different evolutionary models.

Using a Kolmogorov-Smirnov test we are able to determine whether a set of recovered redshifts are from different parent populations. Thus by comparing redshift distributions recovered from datacubes of different sizes we can determine what area of sky is required for SAFARI to be able to reliably distinguish between different evolutionary models. We compare the maximum deviation between the cumulative distributions (Wall 1996) of the redshifts output from our PCC method for skies populated with the burst mode evolution model and with the bright-end evolution model. We perform this comparison for increasing numbers of SPICA FoVs. Using our PCC redshift determination method we find we are able to reliably distinguish (probability that the sources from the two models are drawn from the same distribution,  $P = 0.01\%$ )

between the bright-end and burst mode evolution models with a sky survey area equal to 8 SAFARI FoVs, each of 10 hrs integration time.

## 5. Conclusions

We have found that our PCC redshift determination method is capable of resolving sources (i.e. determining a unique redshift) more than an order of magnitude fainter than the traditional continuum confusion limit, however the efficacy of our method is higher for brighter sources. In this work we have used the PCC method on models based around the SAFARI instrument for SPICA, however the same technique could be used on any sensitive imaging spectrometer. The bright-end and burst mode evolution models include sources up to redshifts of  $z \sim 4$  and 5 respectively. At these redshifts we are still able to determine redshifts for sources using the PCC method. We have not yet tested to see at which redshift the PCC method begins to fail, this may be the subject of future work.

The evolutionary models we have investigated in this work have the bulk of their populations at fluxes fainter than the confusion limit. By employing our PCC method we are therefore greatly increasing the number of galaxies that we are able to uniquely identify in any single observation. This presents us with a better statistical sample with which to compare observed source counts and redshift distributions with those presented in different evolutionary models. We therefore have the potential to reliably distinguish different evolutionary models and our observations with much smaller area surveys, and therefore within shorter observing times.

Future work should include the following: 1) Use of the PAH features to identify sources and determine their redshifts. This will allow us to decrease our spectral resolution, thus increasing instrument sensitivity. 2) Investigation of the viability of taking into account sources

with atypical line strengths. 3) More realistic angular resolution modeling where spatial resolution varies across the waveband. 4) Investigation of the efficiency of the method when implemented on a wider range of evolutionary models. 5) A more quantitative analysis of where our ability to retrieve redshifts from single and combined spectra begins to break down is being conducted. 6) It should also be noted that since the work described in this paper was conducted the technical specifications of SAFARI have changed somewhat (eg. waveband, sensitivity), therefore the results should be re-checked with more up to date modeling of the SAFARI instrument. These topics are currently being investigated.

### Acknowledgements

We would like to thank the anonymous referee for excellent comments and suggestions which markedly improved the clarity of the paper. GR would like to acknowledge an STFC postgraduate studentship, KGI funding from RCUK and DC was funded in part by STFC.

### References

- Armus, L., et al. 2004, *ApJS*, 154, 178  
 Clements, D. L., Isaak, K. G., Madden, S. C., Pearson, C. 2007, *A&A*, 465, 125  
 Dole, H., et al. 2001, *A&A*, 372, 364  
 Dole, H., et al. 2004, *ApJS*, 154, 93  
 Efstathiou, A., Rowan-Robinson, M. 1995, *MNRAS*, 273, 649  
 Efstathiou, A., Rowan-Robinson, M., Siebenmorgen, R. 2000, *MNRAS*, 313, 734  
 Efstathiou, A., Rowan-Robinson, M. 2003, *MNRAS*, 343, 322  
 Elbaz D., et al. 1999, *A&A*, 351, L37  
 Elbaz, D., Cesarsky, C. J., Chanial, P., Aussel, H., Franceschini, A., Fadda, D., Chary, R. R. 2002, *A&A*, 384, 848  
 Förster Schreiber, N. M., Genzel, R., Lutz, D., Kunze, D., Sternberg, A. 2001, *ApJ*, 552, 544  
 Genzel, R., et al. 1998, *ApJ*, 498, 597  
 Hauser, M. G., Dwek, E. 2001, *ARA&A*, 39, 249  
 Jeong, W. -S., Pearson, C. P., Lee, H. M., Pak, S. J., Nakagawa, T. 2006, *MNRAS*, 369, 281  
 Juvela, M., Mattila, K., Lemke, D. 2000, *A&A*, 360, 813  
 Lutz, D., Sturm, E., Genzel, R., Moorwood, A. F. M., Alexander, T., Netzer, H., Sternberg, A. 2000, *ApJ*, 536, 697  
 Negishi, T., Onaka, T., Chan, K. -W., Roellig, T. L. 2001, *A&A*, 375, 566  
 Oliver, S., K., et al. 2000 *MNRAS*, 316, 749  
 Papovich, C., et al. 2004, *ApJS*, 154, 70  
 Pearson, C. P. 2001, *MNRAS*, 325, 1511  
 Pearson, C. P. 2005, *MNRAS*, 358, 1417  
 Pearson, C. P., Jeong, W.-S., Lee, H. M., Nakagawa, T. 2007, *Advances in Space Research*, 40, 605  
 Pearson, C., Khan, S. A. 2009, *MNRAS*, 399, L11  
 Pearson, C. P., Rowan-Robinson, M. 1996, *MNRAS*, 283, 174  
 Pilbratt, G. L. 2004, Presented at the Society of Photo-Optical Instrumentation Engineers (SPIE) Conference, 5481, 401  
 Rowan-Robinson M., Crawford P. 1989, *MNRAS*, 238, 523  
 Rowan-Robinson, M., et al. 2004, *MNRAS*, 351, 1290  
 Rush B., Malkan M., Spinoglio L., 1993, *ApJSS*, 89, 1  
 Saunders, W. et al. 2000, *MNRAS*, 317, 55  
 Scheuer, P. A. G. 1957, *Proceedings of the Cambridge Philosophical Society*, 53, 764  
 Smail, I., Ivison, R. J., Blain, A. W., Kneib, J.-P. 2002, *MNRAS*, 331, 485  
 Smith, J. D. T., et al. 2004, *ApJS*, 154, 199  
 Soifer, B. T., Neugebauer, G. 1991, *AJ*, 101, 354  
 Sturm, E., et al. 1996, *A&A*, 315, L133  
 Sturm, E., Lutz, D., Tran, D., Feuchtgruber, H., Genzel, R., Kunze, D., Moorwood, A. F. M., Thornley, M. D. 2000, *A&A*, 358, 481  
 Sturm, E., Lutz, D., Verma, A., Netzer, H., Sternberg, A., Moorwood, A. F. M., Oliva, E. 2002, *A&A*, 393, 821  
 Swinyard, B., Nakagawa, T., et al. 2009, *Experimental Astronomy*, 23, 193  
 Wall, J. V. 1996, *QJRAS*, 37, 519